

## Current profile redistribution driven by neutral beam injection in a reversed-field pinch

E. Parke, J. K. Anderson, D. L. Brower, D. J. Den Hartog, W. X. Ding, C. A. Johnson, and L. Lin

Citation: *Physics of Plasmas* **23**, 056108 (2016); doi: 10.1063/1.4946019

View online: <http://dx.doi.org/10.1063/1.4946019>

View Table of Contents: <http://scitation.aip.org/content/aip/journal/pop/23/5?ver=pdfcov>

Published by the [AIP Publishing](#)

---

### Articles you may be interested in

[Calibration of an advanced neutral particle analyzer for the Madison Symmetric Torus reversed-field pincha\)](#)

Rev. Sci. Instrum. **83**, 10D704 (2012); 10.1063/1.4729493

[Time-resolved ion energy distribution measurements using an advanced neutral particle analyzer on the MST reversed-field pincha\)](#)

Rev. Sci. Instrum. **83**, 10D302 (2012); 10.1063/1.4728312

[Density fluctuation measurements by far-forward collective scattering in the MST reversed-field pincha\)](#)

Rev. Sci. Instrum. **83**, 10E302 (2012); 10.1063/1.4728098

[Dynamo-free plasma in the reversed-field pinch: Advances in understanding the reversed-field pinch improved confinement modea\)](#)

Phys. Plasmas **12**, 056118 (2005); 10.1063/1.1883666

[Dynamo-free plasma in the reversed field pinch](#)

Phys. Plasmas **11**, L9 (2004); 10.1063/1.1697399

---

PHYSICS  
TODAY

COMPLETELY  
REDESIGNED!



Physics Today Buyer's Guide  
Search with a purpose.

# Current profile redistribution driven by neutral beam injection in a reversed-field pinch

E. Parke,<sup>1,2,a)</sup> J. K. Anderson,<sup>2</sup> D. L. Brower,<sup>1</sup> D. J. Den Hartog,<sup>2</sup> W. X. Ding,<sup>1</sup>  
 C. A. Johnson,<sup>2,3</sup> and L. Lin<sup>1</sup>

<sup>1</sup>Department of Physics and Astronomy, University of California Los Angeles 475 Portola Plaza, Los Angeles, California 90095, USA

<sup>2</sup>Department of Physics, University of Wisconsin-Madison 1150 University Ave., Madison, Wisconsin 53706, USA

<sup>3</sup>Department of Physics, Auburn University 206 Allison Laboratory, Auburn, Alabama 36849, USA

(Received 27 November 2015; accepted 24 February 2016; published online 20 April 2016)

Neutral beam injection in reversed-field pinch (RFP) plasmas on the Madison Symmetric Torus [Dexter *et al.*, Fusion Sci. Technol. **19**, 131 (1991)] drives current redistribution with increased on-axis current density but negligible net current drive. Internal fluctuations correlated with tearing modes are observed on multiple diagnostics; the behavior of tearing mode correlated structures is consistent with flattening of the safety factor profile. The first application of a parametrized model for island flattening to temperature fluctuations in an RFP allows inference of rational surface locations for multiple tearing modes. The  $m=1$ ,  $n=6$  mode is observed to shift inward by  $1.1 \pm 0.6$  cm with neutral beam injection. Tearing mode rational surface measurements provide a strong constraint for equilibrium reconstruction, with an estimated reduction of  $q_0$  by 5% and an increase in on-axis current density of  $8\% \pm 5\%$ . The inferred on-axis current drive is consistent with estimates of fast ion density using TRANSP [Goldston *et al.*, J. Comput. Phys. **43**, 61 (1981)].  
 Published by AIP Publishing. [<http://dx.doi.org/10.1063/1.4946019>]

## I. INTRODUCTION

Neutral beam injection (NBI) is commonly used in tokamaks to drive current and stabilize tearing modes.<sup>1,2</sup> In the Madison Symmetric Torus (MST) reversed field pinch (RFP),<sup>3</sup> neutral beam injection has resulted in stabilization of the core-most tearing (or kink-tearing) modes,<sup>4</sup> but diagnosis of the current profile change has been challenging. Initial estimates from polarimetry profiles indicated an increase of on-axis current density by  $25\% \pm 15\%$ .<sup>5</sup>

Small changes to the equilibrium are more clearly observed by analysis of fluctuation measurements. Tearing mode correlated fluctuations in electron temperature  $\tilde{T}_e$  and line-integrated magnetic field  $\tilde{b}$ , for example, clearly indicate modification of the safety factor profile. An island flattening model for temperature fluctuations has been applied to Thomson scattering measurements on an RFP for the first time, yielding fits in three parameters: temperature gradient  $\nabla T$ , island width  $w$ , and rational surface location  $r_s$ . Changes in  $r_s$  for tearing modes in the core and mid-radius are consistent with current profile peaking. The MSTFit equilibrium solver<sup>6</sup> has been modified to accept rational surface measurements from Thomson scattering; equilibrium reconstruction using rational surface information and polarimetry profiles shows an increase of current density on-axis by  $8\% \pm 5\%$ .

The diagnostic set used for measurements of the safety factor and magnetic field is described in Section II, including both the base diagnostics (Thomson scattering and

interferometry-polarimetry) and meta-diagnostics constructed using integrated data analysis. The island flattening model used to extract rational surface information from the temperature fluctuations is outlined in Section III. Measurements from an ensemble of non-reversed MST discharges are presented, and in Section IV, the results of equilibrium reconstruction with rational surface constraint are given. Diagnosis of current redistribution with neutral beam injection is provided in Section V, with comparison to TRANSP<sup>7</sup> predictions of fast ion deposition.

## II. DIAGNOSTICS

The base diagnostic suite applied to MST discharges in the following analysis consists of edge magnetic coils, including an array of 32 toroidally separated coils for measurement of tearing mode amplitude and phase, as well as a far-infrared (FIR) polarimeter-interferometer and a high-repetition rate Thomson scattering system, both shown in Figure 1. The heterodyne polarimeter-interferometer system on MST consists of 11 vertical chords with 7–8 cm spacing between chords.<sup>8</sup> Three lasers operating at  $432.5 \mu\text{m}$  with  $\sim 0.4$  to  $\sim 1.0$  MHz tuning between each laser provide phase measurements with high-time resolution. The resulting polarimeter-interferometer signals have high bandwidth (200–400 kHz) and allow measurement of dynamic changes in equilibrium density and magnetic field profiles as well as fluctuations associated with tearing modes and other high-frequency activity.

The MST Thomson scattering (TS) system consists of a novel, high-repetition rate laser capable of continuous operation at up to 2 kHz and pulse-burst operation up to 25 kHz;<sup>9,10</sup> filter polychromators and avalanche photodiodes

Note: Paper YI2 2, Bull. Am. Phys. Soc. **60**, 390 (2015).

<sup>a)</sup>Invited speaker.

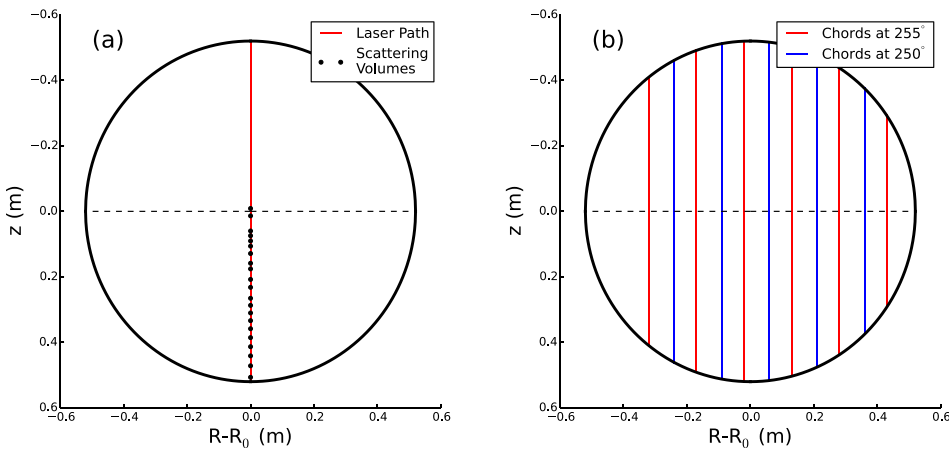


FIG. 1. Poloidal cross-sections showing internal diagnostic coverage: (a) the vertical Thomson scattering chord at 222° toroidal with measurement locations in the lower half of the machine (defined as positive  $z$ ) and (b) the 11 FIR laser chords with 6 chords at 255° toroidal and 5 chords at 250°.

provide sensitive light detection for resolution of temperatures ranging from 10 eV to 5 keV.<sup>11–13</sup> These capabilities allow Thomson scattering to accurately measure the highly dynamic profiles frequently encountered in MST discharges.

Despite the high repetition rates attainable with the Thomson scattering system, most MHD activity remains at or above the Nyquist limit, and electron temperature fluctuation information available through traditional Fourier spectral decomposition is limited to frequencies below the range of interest. This is an information theoretic constraint, however, and correlation techniques that add information permit fluctuation measurements at frequencies well above the Nyquist limit or even the sampling rate for TS data. A striking example of this approach is found in the search for extrasolar planets. Due to weather and limited telescope time, astronomical measurements are frequently both sparsely sampled and irregularly sampled, confounding Fourier analysis. A Bayesian statistical framework has been successfully applied to predict the most likely orbital parameters for identification of candidate exoplanets.<sup>14</sup> Thomson scattering measurements represent a similar, sparsely sampled dataset, with fluctuation contributions from many real, physical sources as well as noise. Forward modeling of electron temperature fluctuations correlated with coherent magnetic structures has likewise been successfully demonstrated as a powerful tool for measuring internal structures associated with MHD activity.<sup>15</sup> In this case, edge magnetic signals with much higher time resolution provide critical additional information; combination of both the magnetic data and electron temperature data under a Bayesian framework makes possible the inference of temperature fluctuations much smaller than the total fluctuation power found in the signal. Since the development of this technique, correlated fluctuation analysis has become a regularly utilized tool for diagnosis of the internal structure of MHD activity in MST.

Using measured temperature data with phase information from the toroidal array (or other diagnostic), temperature fluctuations can be modeled relatively simply as

$$T_e = T_{e,0} + \tilde{T}_{e,(m,n)} \cos(\zeta_{(m,n)} + \delta), \quad (1)$$

where  $T_{e,0}$  is the equilibrium temperature,  $\tilde{T}_{e,(m,n)}$  is the amplitude of temperature fluctuations correlated with a particular mode with poloidal/toroidal mode number  $m/n$ ,  $\zeta_{(m,n)}$  is

the phase of the mode measured by the coil array, and  $\delta$  is a phase offset. The toroidal and poloidal distance between the reference point for the coil array and the Thomson scattering measurement chord contributes a constant phase offset. Due to the Shafranov shift of flux surfaces outward from the vertical chord, core measuring points can also exhibit an apparent phase shift. Additionally, temperature fluctuations out of phase with  $\tilde{b}_\theta$  measured at the wall have a real, non-zero phase offset. These all complicate the analysis of fluctuation phase, but the phase offset  $\delta$  can be treated as a fixed quantity for the purposes of this analysis.

Bayesian analysis in physics is described in detail elsewhere.<sup>16,17</sup> This particular model is described in depth for the particular case where temperature fluctuations are completely in-phase with magnetic perturbations measured at the wall and  $\delta = 0$  in Ref. 15. For fluctuations with  $\delta \neq 0$ , see Ref. 18. By forward modeling with Bayesian analysis, the probability that the fluctuation model fits measured data for a single event can be calculated. Here, a single “event” consists of a burst of Thomson laser pulses, typically spanning  $\sim 200 \mu\text{s}$ , plus toroidal array phase data. Equipped with single-event probability distributions for the parameter of interest,  $\tilde{T}_{e,(m,n)}$ , ensemble analysis of many events consists of straightforward multiplication of the probability distributions to obtain a total probability distribution function (PDF). With sufficiently large ensembles, PDFs with narrow widths are achievable and small amplitude fluctuations are resolvable.

The temperature fluctuations have the form  $A \exp\{i\zeta_{(m,n)}\}$ . Both the real and model fluctuations have the same spatial structure  $(m, n)$  and real frequency  $\omega$  as the magnetic structure rotates past the measurement location. If the model fluctuations are offset by a constant phase  $\exp\{i(\zeta_{(m,n)} - \delta)\}$  from the real fluctuations, then the correlated fluctuation amplitude is given by the inner product of the real fluctuations with the model

$$\langle A \exp\{i\zeta_{(m,n)}\} \exp\{i(\zeta_{(m,n)} - \delta)\} \rangle = A \exp\{i\delta\}. \quad (2)$$

Since the phase offset and fluctuation amplitude are both folded into the correlated amplitude, two correlations at different phases are required to extract this information. Let  $\langle X | \exp\{i(\zeta_{(m,n)} - \delta)\} \rangle$  denote the ensemble averaged correlation of a measured signal,  $X$ , with a model signal. Then, in

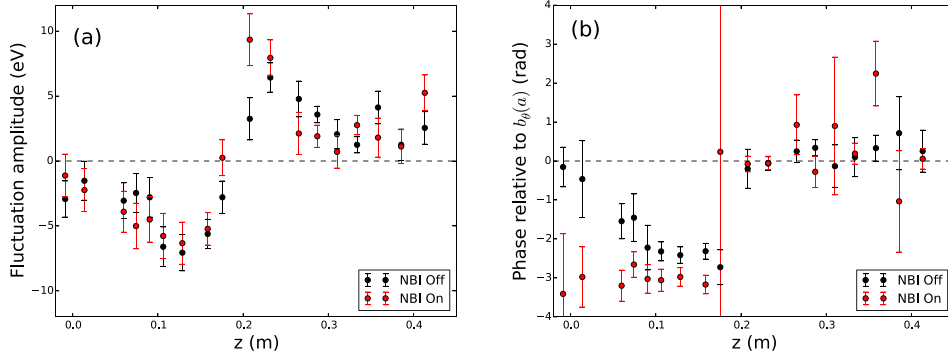


FIG. 2. Amplitude (a) and phase (b) of  $T_e$  fluctuations correlated with  $n=6$  edge magnetic signals without NBI (black) and with NBI (red). The phase flip across the rational surface is accounted for in the amplitude plot by a change in sign. The deviation of the phase at low  $z$  from  $-\pi$  is discussed in Section III C.

analogy with the pseudospectral techniques developed for probe measurements,<sup>19</sup> the two orthogonal correlation amplitudes are

$$\begin{aligned} T &= \langle \tilde{T}_e | \exp\{i\zeta_{(m,n)}\} \rangle \\ T^\dagger &= \langle \tilde{T}_e | \exp\{i(\zeta_{(m,n)} - \pi/2)\} \rangle. \end{aligned} \quad (3)$$

From these correlation amplitudes, the total fluctuation amplitude is

$$\tilde{T}_e = \sqrt{T^2 + (T^\dagger)^2} \quad (4)$$

and the phase offset from  $\tilde{b}_\theta$  is

$$\delta = \tan^{-1}(T^\dagger/T). \quad (5)$$

The errors in the fluctuation amplitude and phase offset are easily determined by propagation of the uncertainties in the correlated amplitudes.

### III. TEARING MODE RATIONAL SURFACE MEASUREMENT WITH THOMSON SCATTERING

Due to the reconnected field lines associated with tearing modes, large islands lead to rapid heat transport. Discharges with tearing mode activity in a variety of devices display a characteristic flattening of the electron temperature profile in the vicinity of the rational surface: tokamaks,<sup>20</sup> stellarators,<sup>21</sup> and the reversed-field pinch.<sup>15</sup> In MST, the islands are generally large enough to overlap, creating stochastic fields and significant particle and heat transport.<sup>22–26</sup> Despite the destruction of flux surfaces by island overlap, temperature flattening due to remnant island structures associated with the tearing modes has been identified on MST.<sup>15</sup>

The generally good agreement between island correlated electron temperature fluctuations and measured  $q$  profiles has been used to suggest equilibrium constraint through this method as well,<sup>27</sup> although for tokamaks core-resonant tearing modes are undesirable for operation and generally only a few are present simultaneously. Pioneering work on JT-60U utilized ECE measurements of island zero-crossings to identify the rational surface location and steer current drive for tearing mode suppression.<sup>1,2</sup> This technique has been applied on other devices, including DIII-D,<sup>28</sup> where comparison of real-time zero-crossing measurements to  $q$  profile reconstructions with MSE demonstrated not only the accuracy of the rational surface measurements but also the potential for improved

performance with lower noise. In the RFP, where tearing modes are present in large numbers and are fundamental to standard discharges, the opportunity for  $q$  profile constraint via island correlated temperature fluctuations is promising.

For MST, the core resonant tearing modes typically have  $n \geq 5$  and  $m = 1$ . The  $n = 5$  mode is frequently the core-most resonant mode, with perturbations in both temperature and magnetic field peaking near the magnetic axis. It is marginally resonant, and plasma conditions in reversed discharges frequently evolve to stabilize this mode. Due to the proximity of the  $n = 5$  structure to the axis, the Shafranov shift of the core-most flux surfaces prevents complete resolution of the temperature structure. Furthermore, the mode amplitude peaks in a region of low shear and the identified temperature structure is consistent with profile peaking rather than island flattening; this has fueled speculation that the mode may be kink-like rather than tearing.<sup>15</sup> For these reasons, the  $n = 5$  rational surface is not identified or used here for equilibrium constraint. Modes with  $n \geq 6$  are more consistently resonant across a variety of discharge conditions and exhibit expected tearing parity in observed structures, see Figure 2.

Temperature fluctuations due to complete island flattening can be expanded in a Fourier series of spatial harmonics,<sup>29</sup>  $\tilde{T}_e = \sum_\nu \delta T_\nu \cos \nu \zeta$ . The harmonic content of the temperature fluctuations is determined by the degree of flattening but generally dominated by the first harmonic. The measurements here represent the first harmonic only, as the predicted and measured amplitudes for the higher harmonics are below experimental error bars for these discharge conditions. Most existing models for helical temperature perturbations associated with tearing modes assume single helicity and intact flux surfaces. For the RFP core, where stochastic overlap erodes island edges and leaves only remnant structures, the correct choice of model is not immediately obvious. In the following analysis, which focuses solely on the  $n = 6$  mode, two different models for the temperature fluctuation are applied: the first harmonic for a completely flattened island developed in Ref. 29 and an adaptation of the model for maximum fluctuation amplitude developed in Ref. 30 for diagnosis of island stability. Both models yield functions of three parameters (temperature gradient, island width  $w$ , and rational surface location  $r_s$ ) which are fit to the Thomson scattering fluctuation measurements via Bayesian inference to obtain the most likely parameter values with error bars. Since the fluctuations are measured over a finite volume, the modeled fluctuation profiles are averaged across

each scattering volume to determine the predicted fluctuation amplitude. This effect turns out to be negligible, however. Additionally, while equilibrium temperature gradients of  $\sim 200$  eV/m are typically observed in these discharges, the fluctuation amplitudes are measured with a greater degree of accuracy than the equilibrium gradient. The temperature gradient is left as a free parameter in the fits, with the most likely values used as a metric for judging the effectiveness of each model in multi-helicity, stochastic plasmas.

For tearing modes with  $n=7$  and 8, the mode amplitudes are lower and the spacing between islands is smaller, leading to smaller remnant structures. The rational surface locations are also further from the magnetic axis, where the scattering volumes average over a larger region. Due to this, the island structures are not sufficiently resolved to apply the model used for the  $n=6$  island structure. The phase flip of temperature fluctuations across the rational surface is clearly visible, however, so the rational surface location is estimated by linear interpolation between the two measurements on either side of the phase flip.

### A. Large island first harmonic model

Ref. 29 solved the heat diffusion equation in the presence of a magnetic island to determine the impact on temperature profiles due to radial heat transport. For a sufficiently large island with complete flattening of the temperature profile, the first harmonic is given by

$$\tilde{T}_e = \frac{\pm w \nabla T_0}{16} \int_0^{\zeta_c} \frac{1 - \cos 2\zeta}{kE(1/k^2)} d\zeta, \quad (6)$$

where  $k^2 = \cos^2(\zeta/2) + 4x^2/w^2$  and  $E(1/k^2)$  is the complete elliptic integral of the second kind. The upper limit of integration is given by  $\zeta_c = \cos^{-1}(1 - 8x^2/w^2)$  if the radial coordinate  $x = r - r_s$  is within the island ( $x < w/2$ ) and  $\pi$  otherwise.  $\nabla T_0$  is the equilibrium gradient (unperturbed by island flattening effects) at the rational surface—it corresponds to the gradient observed at the island X-point.

Fit profiles for discharges without NBI are shown in Figure 3, where only radial locations near the island with sufficient fluctuation power were selected for fitting. The

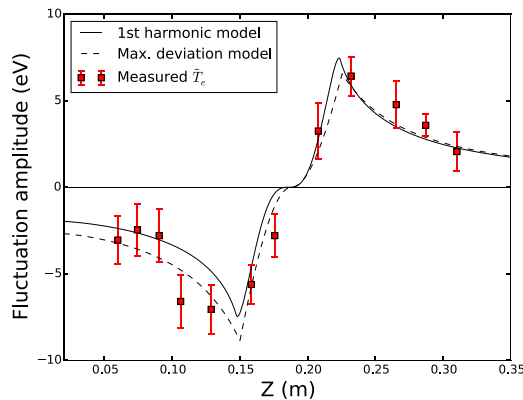


FIG. 3. Helical model fits to  $n=6$  temperature fluctuations without NBI using the first harmonic model (solid) and the maximum temperature deviation model (dashed). Measured fluctuations in the vicinity of the island shown in red.

TABLE I. Large island first harmonic model fit parameters.

Parameter	Min.	Most likely	Max.
$\nabla T_0$ (eV/m)	675	825	1175
$w$ (cm)	6.7	7.4	9.0
$z_s$ (cm)	18.27	18.58	19.46

most likely parameter values are shown in Table I, along with the error bars inferred from the  $1/e$  widths of the probability distributions. For this model, the inferred temperature gradients are much larger than the typical gradients obtained from equilibrium profiles. The probability distributions for the fit parameters also exhibit significant skewness.

### B. Maximum temperature deviation model

The model in Ref. 30 describes the maximum temperature deviation observed as an island rotates past a fixed point of measurement. The version used here neglects the higher order terms used to describe small effects on the temperature fluctuation structure: the ratio of  $B''_\theta$  to  $B'_\theta$  (where the  $'$  denotes the radial derivative) and the linear stability parameter  $\Delta'$ . The extreme values of the flux surfaces (and therefore temperatures) sampled at a fixed volume are obtained alternately when the sampling point is at the helical angle of  $\zeta = \pm\pi$  (the island O-point) or  $\zeta = 0$  (the X-point). For a volume that samples flux surfaces at the radial coordinate  $x$ , the flux surface crossing this volume at the X-point has radial coordinate  $d(x)$  at the O-point (using the notation of Ref. 30). The amplitude of the temperature fluctuations then reduces to  $|dT/dx|_\pm \cdot |d(x) - x|$ , where  $dT/dx$  represents the gradient in the perturbed temperature profile just outside the island at the O-point. The subscript  $\pm$  indicates the dependence on the sign of  $x$ .  $d(x)$  is expressed as

$$d(x) = \pm \sqrt{\frac{w^2}{4} + x^2} \quad (7)$$

and, from Ref. 30, the linear gradient at the O-point is given by

$$\left(\frac{dT}{dx}\right)_\pm = A \left(1 \mp \frac{\pi w}{8r_s}\right), \quad (8)$$

where  $A$  is a constant. Since the gradient for this model is taken at the O-point, while the previous model used the gradient at the X-point, neither  $A$  nor  $dT/dx$  can be directly compared to  $\nabla T_0$ . For a scattering volume that samples only flux surfaces outside the separatrix, this gives a fluctuation amplitude of

$$|\tilde{T}_e| = \left| A \left(1 \mp \frac{\pi w}{8r_s}\right) \right| \cdot \left| \pm \sqrt{\frac{w^2}{4} + x^2} - x \right|. \quad (9)$$

For a scattering volume that samples flux surfaces both inside and outside the separatrix, only the region between  $d(x)$  and the edge of the island,  $x = \pm w/2$ , contributes to the fluctuation amplitude since  $dT/dx = 0$  inside the island

$$|\tilde{T}_e| = \left| A \left( 1 \mp \frac{\pi w'}{8r_s} \right) \right| \cdot \left| \sqrt{\frac{w^2}{4} + x^2} - \frac{w}{2} \right|. \quad (10)$$

Fit profiles for discharges without NBI are shown in Figure 3, where only radial locations near the island with sufficient fluctuation power were selected for fitting. The most likely parameter values are shown in Table II, along with the error bars inferred from the  $1/e$  widths of the probability distributions. The probability distributions for this model's fit parameters are significantly less skewed than the previous model. While the inferred values of the temperature gradient are much closer to the measured values, they are still too large even accounting for the effect of the island perturbation on the temperature profile at the O-point.

### C. Model selection and rational surface measurements

The parameter estimates for both  $w$  and  $r_s$  are in close agreement for the two models tested. The robustness of these parameters against the choice of model provides confidence in the usage of  $r_s$  for measurement of the safety factor profile. The inferred temperature gradient, however, varies significantly between the two models. The failure of both models to accurately predict the equilibrium temperature gradient suggests that a better model is needed to describe discharges with multiple helicity and moderate stochasticity. Since the maximum temperature deviation model results in better fits and the estimated parameters are more consistent with measured equilibria, it is chosen for rational surface measurements. While fits to ECE data have been used to model island flattening behavior in tokamaks,<sup>30</sup> this is the first application of such a model to TS data in an RFP.

A comparison of rational surface measurements for  $n=6, 7$ , and  $8$  is shown in Figure 4 for plasmas both with and without neutral beam heating. All measurements were taken in non-reversed plasmas ( $q(a)=0$ ) with  $I_p=300$  kA and  $n_e \sim 1.0 \times 10^{13} \text{ cm}^{-3}$ . Ensembles with NBI (177 shots) and without NBI (180 shots) were collected over several days, with the discharges on each day alternating between on/off shots for greater similarity between ensembles. For discharges with NBI, the beam was operated with a majority hydrogen mix ( $\sim 95\%$  H,  $5\%$  D) at full power (25 kV, 50 kA). The beam was turned on 12 ms after the start of the discharge (just before the flattop in the current) until 35 ms after the start of the discharge (approximately the end of the flattop).

Thomson data were taken with the lasers in burst mode; each burst consisted of 6 pulses at 25 kHz, with the bursts occurring every millisecond from 22 ms to 26 ms on all shots. During correlation analysis, the bursts were filtered based on plasma conditions: the total plasma current  $I_p$ ; line-

integrated  $n_e$  from either the CO<sub>2</sub> or FIR interferometer; and core-average  $T_e$  from Thomson scattering, from locations with  $z/a < 0.38$ . The amplitude of the  $n=1, m=0$  mode obtained from edge coil signals was used to filter out events occurring too close in time to small bursts of  $m=0$  activity which lead to rapid heat, momentum, and particle transport and drastically alter the equilibrium profiles. Weak filters on tearing mode amplitude and velocity were applied individually for each mode, primarily to avoid correlation with locked mode activity or events where the phase of the mode was not clearly resolved.

The errors in the rational surface location (along the vertical  $z$ -axis) are typically 0.5 cm, and the  $n=6$  rational surface is observed to move inward by  $1.1 \pm 0.6$  cm with NBI. The  $n=7$  and  $8$  rational surfaces likely move outward, but this is obscured by the error bars. These changes are consistent with current redistribution, leading to peaking of the profile.

From Figure 2, the  $n=6$  fluctuation phase relative to  $\tilde{b}_\theta$  at the wall for plasmas without NBI clearly deviates from the  $0$  or  $\pi$  relationship expected of tearing modes. One possible implication of the phase shift is that the parallel heat conductivity may not be high enough to justify the use of an island flattening model. For an equilibrium with intact flux surfaces, this would be a serious concern; in these RFP discharges, however, stochasticity destroys the flux surfaces and weakens the correlation of temperature fluctuations with magnetic perturbations outside the remnant island regions. In the stochastic region between islands, the isothermal surfaces result from a superposition of perturbations due to many modes with different  $n$  values, and the  $0$  or  $\pi$  restriction on the phase of  $\tilde{T}_e$  relative to  $\tilde{b}_\theta$  may not necessarily be guaranteed. In fact, the radial locations with a significant phase shift are all located core-ward of the  $n=6$  island in the stochastic region between the  $n=6$  and  $n=5$  remnant structures. For locations that predominantly sample the remnant  $n=6$  island or locations edge-ward of the island, no significant phase shift is observed. The island flattening model is assumed to still be valid for this case.

### IV. MSTFit AND RATIONAL SURFACE CONSTRAINT

MST equilibria are generally inferred through MSTFit, a two dimensional, axisymmetric Grad-Shafranov solver. Predicted signals are compared to measured values, and the most likely equilibrium profiles are determined through an iterative, least squares minimization via a downhill simplex algorithm. This software package is described in detail elsewhere,<sup>6</sup> so only a brief description of the modifications necessary for rational surface measurements is given here.

In order to accommodate TS rational surface measurements, the calculation of  $\chi^2$  in the comparison of predicted signals to measured data was adapted to include flux surface averaging of the safety factor. Since the TS measurements are ensemble averages of fluctuations correlated with rotating tearing modes, flux surface averaged  $q$  values are the most appropriate comparison rather than local  $q$  values. The local values are less computationally expensive,

TABLE II. Maximum temperature deviation model fit parameters.

Parameter	Min.	Most likely	Max.
A (eV/m)	420	510	660
w (cm)	6.4	7.3	8.4
$z_s$ (cm)	18.31	18.79	19.38

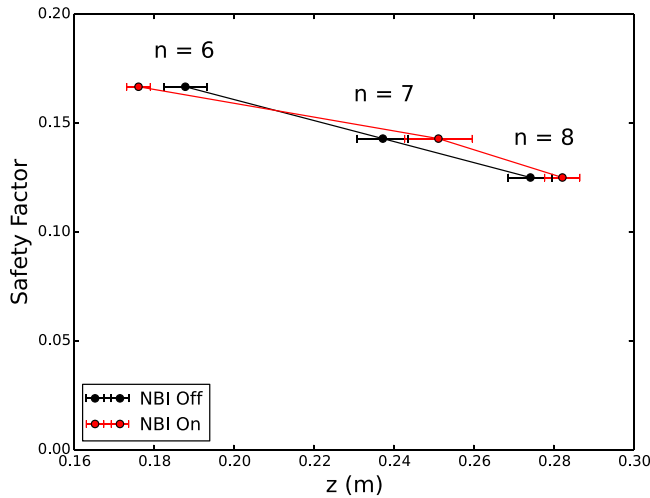


FIG. 4. Rational surface locations for the  $n=6, 7$ , and  $8$  modes with (red) and without (black) NBI. Measurements are along the vertical axis through the geometric center of MST. The range of  $z$ -values shown here covers only the plasma mid-radius.

however, and adding flux surface averaging to each iteration adds significantly (although not prohibitively) to the time required to achieve an equilibrium solution. The flux surface averaged values of  $q$  are projected onto the vertical TS chord for direct comparison with the zero-crossing measurements,  $z_s$ .

Using the measured rational surface locations for the  $n=6-8$  modes with and without NBI, equilibrium reconstruction was performed for all time points where the plasma conditions and tearing mode amplitude/velocity at the wall met the restrictions listed above. Reconstructed profiles with  $q_0 < 1/6$  were rejected as unphysical. The equilibria that passed these filters were averaged to obtain the mean profiles. The error in the reconstruction was estimated as the standard deviation of each parameter over the ensemble of fits.

Shown in Figure 5 are reconstructed profiles for the total magnetic field and the toroidal and poloidal components for the ensemble without NBI. The constraints from the measured

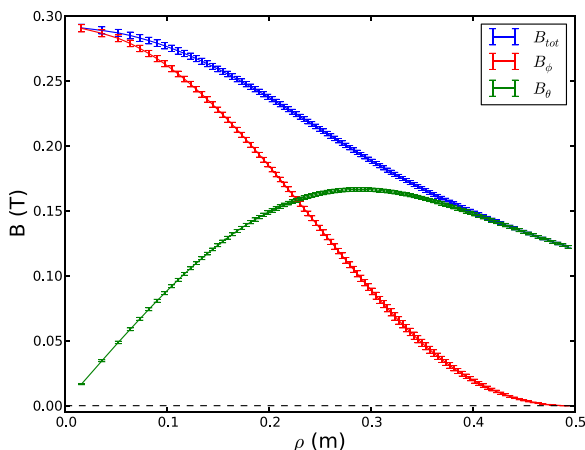


FIG. 5. Reconstructed profiles for the total magnetic field  $B_{tot}$  (blue),  $B_\phi$  (red), and  $B_\theta$  (green) without NBI versus the effective minor radius  $\rho$ . Core magnetic constraint is based solely on TS rational surface measurements.

rational surface locations strongly impact the resulting profiles, with error bars for  $B_{tot}$  less than 1% across the minor radius. Similar profiles are obtained with the ensemble for plasmas with NBI. Aside from the edge coil signals and total plasma current/toroidal flux, the rational surface measurements were the only additional constraint and the only internal constraint on the magnetic field. This demonstrates a high level of precision available even with only a few rational surface measurements.

## V. CURRENT REDISTRIBUTION WITH NBI

While polarimetry measurements suggest an increase in on-axis current density with NBI,<sup>5</sup> the total current does not increase, suggesting current redistribution leading to a profile that is more peaked on axis. This redistribution would reduce the safety factor in the core while increasing it in the mid-radius, flattening the  $q$  profile. The observed shift in rational surfaces obtained from correlated temperature fluctuations (see Figure 4) is consistent with these results. Measurements of  $n=5$  perturbations from interferometry-polarimetry in similar plasma conditions ( $I_p = 300$  kA and  $q(a) = 0$ , but  $n_e \sim 0.7 \times 10^{13}$  cm<sup>-3</sup>) also indicate an inward shift,<sup>5</sup> see Figure 6; the inward movement of the magnetic perturbation is visible both in the Faraday rotation signals and in the toroidal current perturbation inferred through parameterized fits of the Faraday rotation data.

MSTfit equilibrium reconstruction was performed on the ensembles described in Section III with diagnosis from TS rational surface measurements and interferometry-polarimetry profiles. The inferred current and safety factor profiles are plotted in Figures 7 and 8. Although the current in MST typically flows opposite the magnetic field, the absolute values are plotted in Figure 7 for simplicity. Consistent with the estimates from polarimetry alone, the on-axis current density increases with NBI. This increase is offset by a reduction in current density in the mid-radius. The net change in current with NBI ( $J_{\parallel, on} - J_{\parallel, off}$ ) is also plotted in Figure 7. The change in on-axis density corresponds to an increase of  $7.9\% \pm 5.1\%$ . TRANSP modelling of fast ion deposition routinely predicts densities up to 25% of the bulk electron density.<sup>4</sup> This neglects the effect of beam-driven instabilities, however, which limit the fast ion population to lower densities, typically up to 8% of  $n_e$  before the onset of energetic-particle modes. The predicted fast ion density could easily account for the measured change in current on-axis. As a result of redistribution, the current gradient near the magnetic axis increases by nearly a factor of three, while the gradient near the  $n=6$  rational surface increases by  $\sim 20\%-30\%$ . Near the  $n=7$  and  $8$  rational surfaces, the inferred gradient remains roughly the same or decreases slightly. Reconstructed  $q$  profiles, Figure 8, indicate that the observed flattening in the mid-radius corresponds to a reduction of  $q_0$  by  $0.013 \pm 0.007$ . Even without NBI, the inferred profiles indicate marginal resonance of the  $n=5$  mode. With NBI, the rational surface is predicted to be removed from the plasma. Nominally, the loss of the rational surface should damp the  $n=5$  mode. In practice, however, perturbations

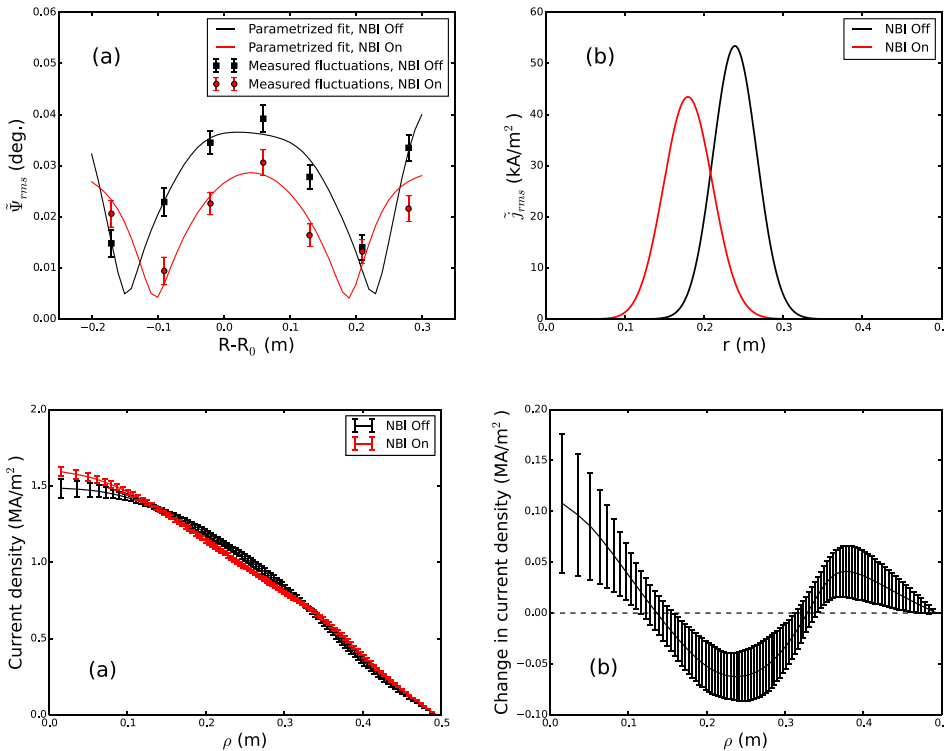


FIG. 6. Fluctuations in Faraday rotation angle correlated with  $n = 5$  perturbation (a) and inferred toroidal current perturbation (b) without NBI (black) and with NBI (red).

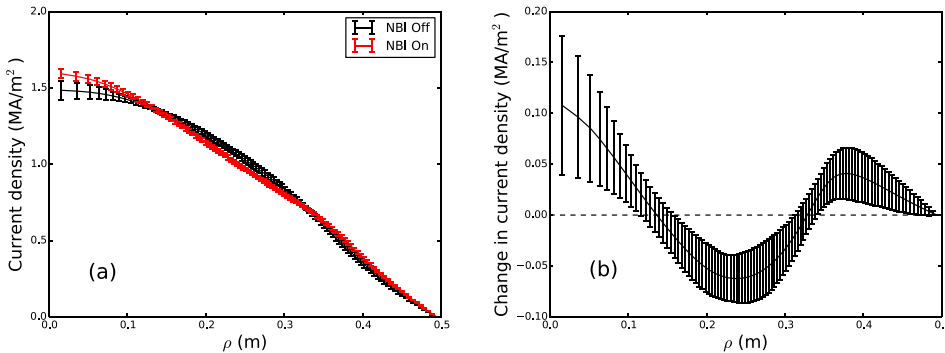


FIG. 7. Reconstructed parallel current profiles (a) without NBI (black) and with NBI (red). Change in parallel current with NBI (b).

with  $n = 5$  structure may still persist while  $q_0$  is in the vicinity of  $1/5$ .

The NBI induced transition from marginal to non-resonance is marked by a reduction in amplitude of the  $n = 5$  mode at the wall,<sup>4</sup> as well as a reduction of internal fluctuations measured by polarimetry<sup>5</sup> and Thomson scattering.<sup>18</sup> The instability is not completely removed, however. Understanding how the  $n = 5$  mode responds to the inferred changes in  $q$  and  $J_{\parallel}$  requires a better understanding of the nature of the  $n = 5$  mode itself. A full evaluation of the impact of the neutral beam on MST plasmas requires measurement of the fast ion distribution, which is not feasible at present. At the large densities estimated by TRANSP, the pressure gradient due to the fast ion population may match or exceed the bulk pressure; normal RFP equilibria are not significantly affected by the bulk pressure, but sufficiently large fast ion

pressure may alter this. Efforts to estimate the fast ion beta and the overall distribution are in progress.

## VI. CONCLUSION

The unique, high-repetition rate Thomson scattering system on MST permits a novel measurement of tearing mode correlated temperature fluctuations. The phase flip in temperature fluctuations associated with island flattening behavior clearly identifies the rational surface location and, for the first time, has been utilized quantitatively for equilibrium reconstruction. High precision reconstructions of internal magnetic field and parallel current profiles are possible with this technique, with relatively small changes in  $J_{\parallel,0}$  ( $\sim 8\%$ ) and  $q_0$  ( $\sim 5\%$ ) clearly resolved in neutral beam heated discharges.

It is worth noting that the full spectrum of tearing mode activity on MST was not utilized for this work. Only the three largest amplitude modes, resonant in the mid-radius, were selected. Given the significant constraint these measurements represent on the equilibrium, this technique may transfer easily to other devices with limited tearing activity. The edge resonant magnetic perturbations utilized on tokamaks may also provide a unique tool to expand this approach.

Furthermore, to accomplish such high precision measurements, relatively large ensembles were required. This was mainly a function of the short burst duration and effective frequency achievable with the current laser system, however. A new laser system capable of much higher repetition rates with more pulses per burst is under development and would significantly reduce the ensemble size required. Already it has demonstrated single shot measurements of rotating island profiles under appropriate conditions. It is feasible that a TS or ECE based island fluctuation diagnostic could contribute to a real time control system.

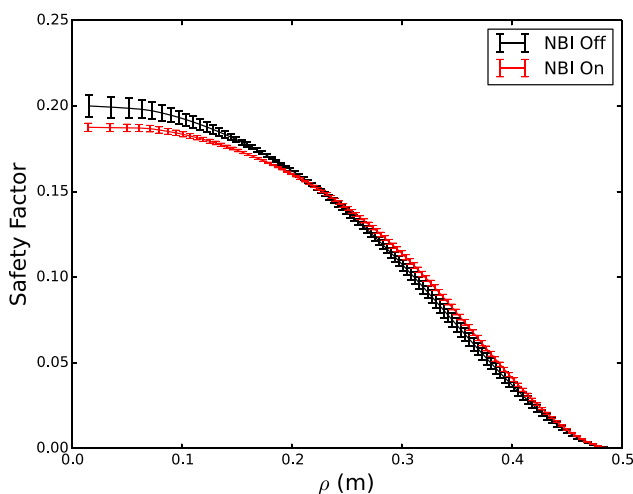


FIG. 8. Safety factor without NBI (black) and with NBI (red).

## ACKNOWLEDGMENTS

This material is based upon work supported by the U.S. Department of Energy Office of Science, Office of Fusion Energy Sciences program under Award Numbers DE-FC02-05ER54814 and DE-FG02-01ER54615. MST data shown in this paper can be obtained in digital format from Ref. 31.

- <sup>1</sup>A. Isayama, Y. Kamada, S. Ide, K. Hamamatsu, T. Oikawa, T. Suzuki, Y. Neyatani, T. Ozeki, Y. Ikeda, K. Kajiwara, and the JT-60 team, *Plasma Phys. Controlled Fusion* **42**, L37 (2000).
- <sup>2</sup>A. Isayama, Y. Kamada, N. Hayashi, T. Suzuki, T. Oikawa, T. Fujita, T. Fukuda, S. Ide, H. Takenaga, K. Ushigusa, T. Ozeki, Y. Ikeda, N. Umeda, H. Yamada, M. Isobe, Y. Narushima, K. Ikeda, S. Sakakibara, K. Yamazaki, K. Nagasaki, and the JT-60 Team, *Nucl. Fusion* **43**, 1272 (2003).
- <sup>3</sup>R. N. Dexter, D. W. Kerst, T. W. Lovell, S. C. Prager, and J. C. Sprott, *Fusion Sci. Technol.* **19**, 131 (1991).
- <sup>4</sup>J. K. Anderson, A. F. Almagri, D. J. Den Hartog, S. Eilerman, C. B. Forest, J. J. Koliner, V. V. Mirnov, L. A. Morton, M. D. Normberg, E. Parke, J. A. Reusch, J. S. Sarff, J. Waksman, V. Belykh, V. I. Davydenko, A. A. Ivanov, S. V. Polosatkin, Y. A. Tsidulko, L. Lin, D. Liu, G. Fiksel, H. Sakakita, D. A. Spong, and J. Titus, *Phys. Plasmas* **20**, 056102 (2013).
- <sup>5</sup>L. Lin, W. X. Ding, D. L. Brower, J. J. Koliner, S. Eilerman, J. Reusch, J. K. Anderson, A. F. Almagri, B. E. Chapman, M. D. Normberg, J. S. Sarff, J. Waksman, and D. Liu, *Bull. Am. Phys. Soc.* **57**, JP8.137 (2012).
- <sup>6</sup>J. Anderson, C. Forest, T. Biewer, J. Sarff, and J. Wright, *Nucl. Fusion* **44**, 162 (2004).
- <sup>7</sup>R. J. Goldston, D. C. McCune, H. H. Towner, S. L. Davis, R. J. Hawryluk, and G. L. Schmidt, *J. Comput. Phys.* **43**, 61 (1981).
- <sup>8</sup>D. L. Brower, W. X. Ding, S. D. Terry, J. K. Anderson, T. M. Biewer, B. E. Chapman, D. Craig, C. B. Forest, S. C. Prager, and J. S. Sarff, *Rev. Sci. Instrum.* **74**, 1534 (2003).
- <sup>9</sup>D. J. Den Hartog, J. R. Ambuel, M. T. Borchardt, J. A. Reusch, P. E. Robl, and Y. M. Yang, *J. Phys.: Conf. Ser.* **227**, 012023 (2010).
- <sup>10</sup>J. A. Reusch, M. T. Borchardt, D. J. Den Hartog, A. F. Falkowski, D. J. Holly, R. O'Connell, and H. D. Stephens, *Rev. Sci. Instrum.* **79**, 10E733 (2008).
- <sup>11</sup>H. D. Stephens, M. T. Borchardt, D. J. Den Hartog, A. F. Falkowski, D. J. Holly, R. O'Connell, and J. A. Reusch, *Rev. Sci. Instrum.* **79**, 10E734 (2008).
- <sup>12</sup>T. N. Carlstrom, J. DeBoo, R. Evanko, C. M. Greenfield, C. L. Hsieh, R. T. Snider, and P. Trost, *Rev. Sci. Instrum.* **61**, 2858 (1990).
- <sup>13</sup>C. L. Hsieh, J. Haskovec, T. N. Carlstrom, J. C. DeBoo, C. M. Greenfield, R. T. Snider, and P. Trost, *Rev. Sci. Instrum.* **61**, 2855 (1990).
- <sup>14</sup>P. C. Gregory, *Astrophys. J.* **631**, 1198 (2005).
- <sup>15</sup>H. D. Stephens, D. J. Den Hartog, C. C. Hegna, and J. A. Reusch, *Phys. Plasmas* **17**, 056115 (2010).
- <sup>16</sup>U. von Toussaint, *Rev. Mod. Phys.* **83**, 943 (2011).
- <sup>17</sup>D. Sivia and J. Skilling, *Data Analysis: A Bayesian Tutorial* (Oxford Science Publications, Oxford University Press, 2006).
- <sup>18</sup>E. Parke, "Diagnosis of equilibrium magnetic profiles, current transport, and internal structures in a reversed-field pinch using electron temperature fluctuations," Ph.D. thesis (University of Wisconsin-Madison, 2014).
- <sup>19</sup>T. D. Tharp, "Measurements of nonlinear Hall-driven reconnection in the reversed field pinch," Ph.D. thesis (University of Wisconsin-Madison, 2010).
- <sup>20</sup>M. Nave, A. Edwards, K. Hirsch, M. Hugon, A. Jacchia, E. Lazzaro, H. Salzmann, and P. Smeulders, *Nucl. Fusion* **32**, 825 (1992).
- <sup>21</sup>R. Jaenicke and W. V.-A. Team, *Nucl. Fusion* **28**, 1737 (1988).
- <sup>22</sup>A. B. Rechester and M. N. Rosenbluth, *Phys. Rev. Lett.* **40**, 38 (1978).
- <sup>23</sup>B. V. Chirikov, *Phys. Rep.* **52**, 263 (1979).
- <sup>24</sup>S. Hokin, A. Almagri, S. Assadi, J. Beckstead, G. Chartas, N. Crocker, M. Cudzinovic, D. Den Hartog, R. Dexter, D. Holly, S. Prager, T. Rempel, J. Sarff, E. Scime, W. Shen, C. Spragins, C. Sprott, G. Starr, M. Stoneking, C. Watts, and R. Nebel, *Phys. Fluids B* **3**, 2241 (1991).
- <sup>25</sup>N. E. Lanier, D. Craig, J. K. Anderson, T. M. Biewer, B. E. Chapman, D. J. Den Hartog, C. B. Forest, S. C. Prager, D. L. Brower, and Y. Jiang, *Phys. Rev. Lett.* **85**, 2120 (2000).
- <sup>26</sup>T. M. Biewer, C. B. Forest, J. K. Anderson, G. Fiksel, B. Hudson, S. C. Prager, J. S. Sarff, J. C. Wright, D. L. Brower, W. X. Ding, and S. D. Terry, *Phys. Rev. Lett.* **91**, 045004 (2003).
- <sup>27</sup>J. Berrino, E. Lazzaro, S. Cirant, G. D'Antona, F. Gandini, E. Minardi, and G. Granucci, *Nucl. Fusion* **45**, 1350 (2005).
- <sup>28</sup>Y. S. Park and A. S. Welander, *Plasma Phys. Controlled Fusion* **48**, 1447 (2006).
- <sup>29</sup>R. Fitzpatrick, *Phys. Plasmas* **2**, 825 (1995).
- <sup>30</sup>C. Ren, J. D. Callen, T. A. Gianakon, C. C. Hegna, Z. Chang, E. D. Fredrickson, K. M. McGuire, G. Taylor, and M. C. Zarnstorff, *Phys. Plasmas* **5**, 450 (1998).
- <sup>31</sup>See supplementary material at <http://dx.doi.org/10.1063/1.4946019> for the digital format of the data shown in this paper.